

GRADIENT-BASED TWO-SCALE TOPOLOGY OPTIMIZATION  
WITH B-SPLINES ON SPARSE GRIDS\*JULIAN VALENTIN<sup>†</sup>, DANIEL HÜBNER<sup>‡</sup>, MICHAEL STINGL<sup>‡</sup>, AND DIRK PFLÜGER<sup>†</sup>

**Abstract.** Structural optimization searches for the optimal shape and topology of components such that specific physical quantities are optimized, for instance, the stability of the resulting structure. Problems involving multiple scales, i.e., structures on a microscopic and a macroscopic level, can be efficiently solved by homogenization-based two-scale approaches. In each optimization iteration, many computationally expensive tensors  $E$  describing the macroscopic behavior of a given microstructure have to be calculated, implying that the solution of one optimization problem can take weeks. The computational complexity can be greatly reduced with surrogates  $\tilde{E}$  that are constructed in advance in an offline phase via interpolation and that can be reused for different scenarios. Three main issues arise in this context: First, the curse of dimensionality renders conventional interpolation schemes infeasible even for moderate dimensionalities  $> 4$ . Therefore, we use sparse grid interpolation combined with a novel problem-tailored boundary treatment to drastically reduce the necessary grid size with only slightly higher approximation errors. Second, common sparse grid bases are not continuously differentiable. Hierarchical B-splines achieve lower approximation errors and supply exact continuous gradients of  $\tilde{E}$ , which enables gradient-based optimization without approximating gradients of  $E$ . Third, the interpolated tensors are usually required to be positive definite, which is not fulfilled by common interpolation methods. We are able to preserve positive definiteness of the interpolated tensors by interpolating Cholesky factors instead. Combining these three contributions allows computing optimized structures for two- and three-dimensional optimization scenarios with speedups of up to 86 when compared to non-surrogate-based solutions.

**Key words.** topology optimization, two scale, sparse grids, B-splines

**AMS subject classifications.** 65D05, 65D07, 74P05, 74P15

**DOI.** 10.1137/19M128822X

**1. Introduction.** In recent years, making parts with additive manufacturing (e.g., 3D printers) became increasingly important in research and industry. The main advantage, when compared to conventional manufacturing methods, is the large freedom of design in the shape or topology of components, which allows for detailed structures with a fine resolution. A suitable approach to tailor such parts for specific needs is two-scale optimization, in which optimization problems are formulated as material distribution problems using composite materials. In detail, given a domain  $\Omega \in \mathbb{R}^d$  we search for a structure that is contained in the domain and optimal with respect to a given cost functional subject to some constraints. The structure is assumed to consist of composites or lattices (which are composites of material and void) that are presumed to be periodic on a microscopic length-scale. Thus, the microstructure

---

\*Submitted to the journal's Computational Methods in Science and Engineering section September 19, 2019; accepted for publication (in revised form) June 12, 2020; published electronically August 24, 2020.

<https://doi.org/10.1137/19M128822X>

**Funding:** This work was supported by the Ministry of Science, Research and the Arts of the State of Baden-Württemberg and by the Deutsche Forschungsgemeinschaft (DFG, German Research Foundation) – Project-ID 61375930 – SFB 814 – “Additive Manufacturing,” Subproject C02, and by the Deutsche Forschungsgemeinschaft (DFG, German Research Foundation) under Germany’s Excellence Strategy – EXC 2075 – 390740016.

<sup>†</sup>Institute for Parallel and Distributed Systems (IPVS), University of Stuttgart, Germany (julian.valentin@ipvs.uni-stuttgart.de, dirk.pflueger@ipvs.uni-stuttgart.de).

<sup>‡</sup>Department of Mathematics, FAU Erlangen-Nürnberg, Germany (daniel.huebner@fau.de, michael.stingl@fau.de).

can be described by periodic functions, which are fully characterized by their values on a unit cell. We restrict ourselves to two- and three-dimensional settings in linear elasticity in this article for the sake of simplicity. However, the proposed method is applicable to general two-scale optimization.

Several methods have been developed to tackle problems on different length scales. In this article, we use the well-established theory of asymptotic homogenization [1, 12, 19, 33, 43], which is preferable over standard mechanic approaches as shown by Hollister and Kikuchi [30]. Based on the work by Murat and Tartar in the late 1970s numerical algorithms using this method evolved slowly (see, e.g., [23, 24, 35]) until Bendsøe and Kikuchi [8] presented an efficient approach in their seminal paper on topology optimization, and it is now widely used in concurrent design of the topology of micro- and macrostructures [40, 27, 13, 36, 37, 49, 16, 31, 42, 6, 4, 21]. The method assumes that the macroscopic behavior of a microstructure can be described by effective material properties, which can be derived by solving partial differential equation problems on unit cells. Hence, both the macro- and microscale are involved in the optimization problem, and solving this coupled two-scale problem, e.g., with a hierarchical solution strategy like Rodrigues, Guedes, and Bendsøe [40], will generally result in a high computational cost due to many repetitive local material optimizations. To circumvent this issue, one can subdivide the macroscopic domain into subdomains, each with a uniform microstructure [42], or, in the extreme case, use a uniform microstructure everywhere [36, 37, 50].

However, Bendsøe and Kikuchi already mention that the scales can effectively be decoupled at the cost of losing design freedom by restricting the space of admissible unit cell topologies. For this, they introduce a parametrization of the topology in the unit cell with  $r$  parameters and calculate the homogenized properties for a discrete and bounded set of parameter values. This stage is independent of the employed optimization procedure itself and can thus be called the *offline phase*. During the *online phase*, the optimization problem on the macroscopic scale is solved, where the design variables are the parameters of the microstructure and the complete dependence of the local material properties on the parameters is approximated by interpolation in the parameter space, which is a subset of  $\mathbb{R}^r$ . Note that for the use of gradient-based optimization methods the interpolating function should be continuously differentiable on the whole parameter space. The parametrization of Bendsøe and Kikuchi consists of three values: Two parameters describe the width and height of a rectangular (void) inclusion in solid material, which is inspired by rank-2 laminates, which have proven to be optimal microstructures for single-load problems in two dimensions [2]. The third value characterizes the rotation of the microstructure and does not have to be considered during homogenization, but can be applied to the homogenized properties themselves. This leads to a two-dimensional parameter space for the interpolation, which can easily be performed by, e.g., Legendre polynomials. A similar approach is conducted in the work by Xia and Breitkopf [48], where the authors use the multi-dimensional cubic spline interpolation from Habermann and Kindermann [28] for the stress-strain relationship of structures with nonlinear material phases.

Using such a decoupled two-scale approach one usually encounters the problem of nonconnectivity during the reconstruction of the structures, i.e., the microstructure in one unit cell might not easily be connected to the one in an adjacent unit cell. This will not only result in poor manufacturability but also lead to deviation of the effective properties estimated by the homogenization procedure and load transition issues in the structure. There have recently been contributions to tackle this important challenge, which employ a careful posttreatment of the optimization result [38, 3, 26]

or add additional constraints to the optimization problem [17]. However, we will neglect that issue in this article, as the focus resides on other challenges.

The aforementioned interpolation schemes on common, i.e., full or equidistant, grids suffer from the *curse of dimensionality* [7]: The number of grid points grows exponentially with the dimensionality  $r$  of the parameter space. (Note that this is not the spatial dimension of the design space  $d$ .) Thus, these approaches are computationally infeasible for  $r > 4$ . Sparse grids are known to ease this curse to some extent [11]. We will present an interpolation scheme using spatially adaptively generated sparse grids, since there are regions of the elasticity tensor with different characteristics (e.g., the second derivatives have different order of magnitudes in different regions).

Common sparse grid bases, such as the well-known piecewise linear hat functions or piecewise polynomial functions by Bungartz [10], share the shortcoming of having discontinuous derivatives. Hierarchical B-splines on sparse grids have been employed successfully, for example, in data mining [39] or optimization [46]. They generalize the hat functions to a continuously differentiable basis if the B-spline degree  $p$  is chosen to be larger than one. The continuous derivatives can be evaluated explicitly and efficiently. As a result, the objective function can be differentiated with respect to the parameters, enabling us to use gradient-based optimization methods, which greatly increases the speed of convergence.

We have shown the general feasibility of B-splines on sparse grids for two-scale topology optimization in previous work [32, 46]. However, in these papers, we considered only simple parametrizations for the unit cell topology with at most three parameters in only two-dimensional optimization settings. Consequently, it was sufficient to employ regular sparse grids. In the present paper, we want to pave the way for considerably more complex parametrizations for two- and three-dimensional optimization settings, for which spatial adaptivity of the sparse grids is crucial. In addition, in [46], the optimization algorithm experienced numerical difficulties if the level of the underlying regular sparse grid was not high enough. Optimized structures could not be obtained in these cases, which also occurred for most spatially adaptive sparse grids. This paper shows that the root cause of this behavior is the non-positive-definiteness of the interpolated elasticity tensors. To solve this problem, we propose a spatially adaptive interpolation scheme that preserves the positive definiteness as well as the explicit continuous differentiability of the elasticity tensors.

The rest of this article is structured as follows: We first recall the two-scale approach using homogenization in section 2. In section 3, we repeat the notion of hierarchical B-splines on sparse grids and elaborate on spatially adaptive generation of sparse grids with proper treatment of the boundary. We will continue by focusing on the preservation of the positive definiteness of elasticity tensors in section 4. Numerical results for two- and three-dimensional cantilevers will be given in section 5, along with convergence studies and error plots. Finally, we summarize our results and give an outlook in section 6.

**2. Two-scale approach.** The problems at the micro- and macroscopic scales are well-known [9, 41]; however, we briefly recall the basics for the sake of completeness.

Let a macroscopic domain  $\Omega$  be discretized by quadrilateral (in two dimensions (2D)) or hexahedral (in three dimensions (3D)) finite elements  $Y_n$ ,  $n = 1, \dots, \mathcal{N}_{\text{cell}}$  (see Figure 1), and let  $\mathcal{N}$  denote the degrees of freedom, i.e., the number of nodes of the finite element mesh times the spatial dimension. We identify each finite element with exactly one unit cell and drop the index  $n$  in the remainder for better readability.

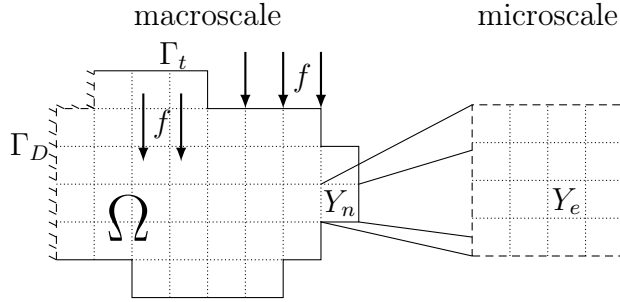


FIG. 1. Finite element meshes at the macro- and microscopic level. A macroscopic domain  $\Omega$  with Dirichlet boundary  $\Gamma_D$  and Neumann boundary  $\Gamma_t$  is discretized into  $N_{\text{cell}}$  finite elements  $Y_n$ . Each finite element is discretized itself by  $M_{\text{cell}}$  finite elements  $Y_e$  on a microscopic level.

ity purpose, whenever it is possible without losing clarity. In  $f \in \mathbb{R}^{\mathcal{N}}$  we combine distributed loads and tractions, where the latter only apply at some part  $\Gamma_t \subset \partial\Omega$  of the boundary. Displacement components may be specified on the other part  $\Gamma_D$  of the boundary. The macroscopic displacement itself will be denoted by  $u \in \mathbb{R}^{\mathcal{N}}$ . Furthermore, we call a function  $Y$ -periodic if it takes equal values at opposite faces of  $Y$ . Note that for this property,  $Y$  does not have to be a square or cube, respectively, but other geometric shapes, like, e.g., parallelograms or parallelepipeds, are possible as well [5, 32].

Let an admissible set  $U_{\text{ad}}$ , which will be defined later, and an objective functional  $J: \mathbb{R}^{\mathcal{N}} \times U_{\text{ad}} \rightarrow \mathbb{R}$  be given. The discretized problem on the macroscopic scale then reads as

$$(2.1) \quad \begin{aligned} & \min_{\boldsymbol{x} \in U_{\text{ad}}} J(u, \boldsymbol{x}) \\ & \text{s.t. } K(\boldsymbol{x})u = f \end{aligned}$$

with design variables  $\boldsymbol{x}$  and stiffness matrix  $K \in \mathbb{R}^{\mathcal{N} \times \mathcal{N}}$ , which depends on the material properties given by  $\boldsymbol{x}_n$  in each finite element  $Y_n$ .

To solve problem (2.1), we first calculate the effective material properties in each unit cell  $Y := Y_n$  for a fixed topology using asymptotic homogenization. For this, let  $Y$  be discretized in turn by finite elements  $Y_e$ ,  $e = 1, \dots, M_{\text{cell}}$ , and  $\mathcal{M}$  denote the degrees of freedom on the microscopic level. Further, let the  $Y$ -periodic unit cell topology be characterized by a parametrization with  $r$  parameters

$$(2.2) \quad \begin{aligned} P_n: [0, 1]^r & \rightarrow (\mathbb{R}^{3 \times 3 \times 3 \times 3})^{M_{\text{cell}}}, \\ \boldsymbol{x}_n & \mapsto (E_1, E_2, \dots, E_{M_{\text{cell}}}), \end{aligned}$$

where  $\boldsymbol{x}_n \in [0, 1]^r$  is a set of parameter values for cell  $Y$  and  $E_e$  is the fourth-order stiffness tensor related to the material properties in the microscopic finite element  $Y_e$ . For simplicity, we restrict ourselves to  $P_n = P$  for all  $n = 1, \dots, N_{\text{cell}}$ , i.e., each unit cell is parametrized in the same way. Some examples of parametrizations will be given in subsection 5.1. Of course, even if the parametrization is the same for all unit cells,  $\boldsymbol{x}_n$  might differ from cell to cell leading to different realizations of  $P$ , i.e., microstructures.

The problem on the microscopic scale is then to solve finite element problems

$$(2.3) \quad K_Y(P(\boldsymbol{x}_n)) \chi^{kl} = f^{kl}$$

for  $Y$ -periodic microscopic displacement fields  $\chi^{kl} \in \mathbb{R}^{\mathcal{M}}$ ,  $k, l = 1, 2, 3$ , with stiffness matrix  $K_Y$  depending on the topology in  $Y$  and hence on  $P(\mathbf{x}_n)$ . The right-hand sides are given by

$$(2.4) \quad f^{kl} = \sum_e \int_{Y_e} B_e^\top E_e \epsilon^{0(kl)} \, dy ,$$

where  $B_e$  is the finite element strain-displacement matrix and  $\epsilon^{0(kl)}$  are unit test strain fields. The effective material tensor for unit cell  $Y$  is then given by

$$(2.5) \quad \begin{aligned} E_{ijkl}^H(\mathbf{x}_n) &= \frac{1}{|Y|} \sum_e \left( \chi^{0(ij)} - \chi^{ij} \right)^\top \int_{Y_e} B^\top E_e(\mathbf{x}_n) B \, dy \left( \chi^{0(kl)} - \chi^{kl} \right) \\ &= \frac{1}{|Y|} \sum_e \left( \chi^{0(ij)} - \chi^{ij} \right)^\top K_e(\mathbf{x}_n) \left( \chi^{0(kl)} - \chi^{kl} \right), \end{aligned}$$

where  $\chi^{0(ij)}$  is the nodal displacement vector corresponding to test strain field  $\epsilon^{0(ij)}$ . Note that due to its symmetry the fourth-order tensor  $E^H$  can be expressed in Voigt notation [47] by a second-order tensor  $E^H \in \mathbb{R}^{6 \times 6}$ .

On the macroscopic level, i.e., in problem (2.1), the design  $\mathbf{x} = (\mathbf{x}_1, \dots, \mathbf{x}_{\mathcal{N}_{\text{cell}}})$  is a combination of the parameter values in all unit cells, and the space of admissible design variables is given by  $U_{\text{ad}} \subseteq ([0, 1]^r)^{\mathcal{N}_{\text{cell}}}$ . The global stiffness matrix  $K$  is assembled from the local ones depending on the homogenized material tensors:

$$(2.6) \quad K(\mathbf{x}) = \bigwedge_{n=1}^{\mathcal{N}_{\text{cell}}} K_{Y_n}(E^H(\mathbf{x}_n)) .$$

In the numerical studies at the end of the article, we seek to minimize the compliance. Additionally, we add an upper bound  $V_0$  for the material volume fraction to exclude the trivial solution with solid material. The volume  $V$  of the macrostructure is computed with respect to the local porosity of the microstructure, which of course depends on the local values of the parameters. Thus, the macroscopic problem is given by

$$(2.7) \quad \begin{aligned} \min_{\mathbf{x} \in U_{\text{ad}}} \quad & f^\top u \\ \text{s.t.} \quad & K(\mathbf{x})u = f, \\ & V(\mathbf{x}) \leq V_0 . \end{aligned}$$

**3. B-splines on sparse grids.** In this section, we briefly introduce the hierarchical B-spline basis on sparse grids.

**3.1. Cardinal B-splines.** We recall the basic properties of B-splines, adopting the notation of [29]. The cardinal (parent) B-spline  $b^p: \mathbb{R} \rightarrow \mathbb{R}$  of degree  $p \in \mathbb{N}_0$  is defined by

$$(3.1) \quad b^p(x) := \int_0^1 b^{p-1}(x-y) \, dy , \quad p > 1 ,$$

starting with the indicator function  $b^0 := \chi_{[0,1]}$  of the interval  $[0, 1]$ . It is well-known [29] that  $b^p$  is bounded ( $0 \leq b^p \leq 1$ ), symmetric ( $b^p(x) = b^p(p+1-x)$ ), and compactly supported ( $\text{supp } b^p = [0, p+1]$ ). On  $[k, k+1]$ ,  $k = 0, \dots, p$ ,  $b^p$  is a polynomial of

degree  $p$ , while satisfying  $b^p \in C^{p-1}(\mathbb{R})$ .  $b^p$  can also be defined via the Cox–de Boor recurrence formula [14, 15]

$$(3.2) \quad b^p(x) = \frac{x}{p} b^{p-1}(x) + \frac{p+1-x}{p} b^{p-1}(x-1), \quad p > 1.$$

The translates  $b^p(\cdot - k)$ ,  $k \in \mathbb{Z}$ , form a basis of the spline space on  $\mathbb{Z}$ , i.e., the space of all piecewise (with respect to  $\mathbb{Z}$ ) polynomials of degree  $\leq p$  that are at least  $p-1$  times continuously differentiable.

**3.2. Hierarchical B-splines.** We repeat the definition of hierarchical B-splines on sparse grids [46]. For level  $\ell \in \mathbb{N}$  and index  $i \in I_\ell$  with  $I_\ell := \{1, 3, 5, \dots, 2^\ell - 1\}$ , we define the hierarchical B-spline  $\varphi_{\ell,i}^p : [0, 1] \rightarrow \mathbb{R}$  by

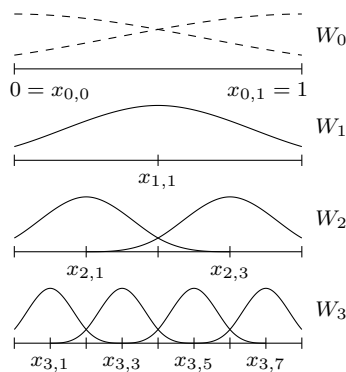
$$(3.3) \quad \varphi_{\ell,i}^p(x) := b^p\left(\frac{x}{h_\ell} + \frac{p+1}{2} - i\right), \quad h_\ell := 2^{-\ell}.$$

In Figure 2(a), the hierarchical B-splines up to level 3 are shown for the cubic case. In the following, we fix the degree with  $p = 3$  and omit the corresponding superscript in  $\varphi_{\ell,i}^p$ . We assume that  $p$  is odd since otherwise the knots of the B-splines (the locations where the B-splines are not infinitely many times differentiable) are not nested. Note that for  $p = 1$ , we obtain the common hat function basis. We continue with the nodal subspace  $V_\ell$  and the hierarchical subspace  $W_\ell$ :

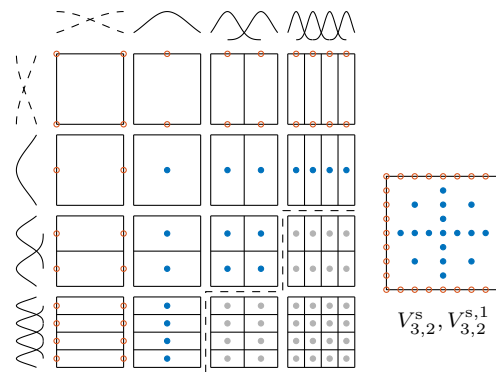
$$(3.4) \quad \begin{aligned} V_\ell &:= \text{span}\{\varphi_{\ell,i} \mid i = 1, \dots, 2^\ell - 1\}, \\ W_\ell &:= \text{span}\{\varphi_{\ell,i} \mid i \in I_\ell\}. \end{aligned}$$

For  $p = 1$ , it can be proven easily [44] that

$$(3.5) \quad V_\ell = \bigoplus_{\ell'=1}^{\ell} W_{\ell'}.$$



(a) Hierarchical B-spline basis in one dimension with boundary functions (dashed).



(b) Regular sparse grid of level 3 without boundary ( $V_{3,2}^s$ : only the  $\bullet$  points) and with boundary ( $V_{3,2}^{s,1}$ :  $\bullet$  and  $\circ$  points). The rectangles indicate  $\text{supp } \varphi_{\ell,i}$ .

FIG. 2. Hierarchical cubic B-splines ( $p = 3$ ) on sparse grids.

In [45, 46], we have shown that this relation also holds for odd degrees  $p > 1$  when restricting all functions involved to

$$D_\ell := \left[ \frac{p+1}{2} h_\ell, 1 - \frac{p+1}{2} h_\ell \right] .$$

With each basis function  $\varphi_{l,i}$ , we associate a grid point

$$(3.6) \quad x_{\ell,i} := i \cdot h_\ell \in [0, 1] ,$$

which coincides with the center of the support of  $\varphi_{\ell,i}$ .

**3.3. Multivariate B-splines and regular sparse grids.** For  $r \in \mathbb{N}$  dimensions, we define the index set  $I_\ell$  for level  $\ell \in \mathbb{N}^r$  as

$$(3.7) \quad I_\ell := I_{\ell_1} \times \cdots \times I_{\ell_r} .$$

The  $r$ -variate hierarchical B-spline  $\varphi_{\ell,i}: [0, 1]^r \rightarrow \mathbb{R}$  of level  $\ell \in \mathbb{N}^r$  and index  $i \in I_\ell$  is defined as the tensor product of one-dimensional B-splines,

$$(3.8) \quad \varphi_{\ell,i}(\mathbf{x}) := \prod_{t=1}^r \varphi_{\ell_t, i_t}(x_t) .$$

The associated grid point is simply

$$(3.9) \quad \mathbf{x}_{\ell,i} := (x_{\ell_1, i_1}, \dots, x_{\ell_r, i_r}) \in [0, 1]^r ,$$

and the multivariate counterparts of the subspaces are given by

$$(3.10) \quad \begin{aligned} V_\ell &:= \text{span}\{\varphi_{\ell,i} \mid \mathbf{i} \leq \mathbf{2}^\ell - \mathbf{1}\} , \\ W_\ell &:= \text{span}\{\varphi_{\ell,i} \mid \mathbf{i} \in I_\ell\} , \end{aligned}$$

where operators and operations are to be read componentwise (i.e.,  $1 \leq i_t \leq 2^{l_t} - 1$  for all  $t = 1, \dots, r$ ). As in [46], we can generalize the relation (3.5) to

$$(3.11) \quad V_\ell = \bigoplus_{\mathbf{1} \leq \ell' \leq \ell} W_{\ell'} \quad \text{on} \quad D_\ell := D_{\ell_1} \times \cdots \times D_{\ell_r} .$$

Given a function  $f: [0, 1]^r \rightarrow \mathbb{R}$  to be interpolated and a set  $L \subset \mathbb{N}^r$  of levels, we define the following interpolation problem: Find  $\alpha_{\ell,i} \in \mathbb{R}$  for  $\ell \in L$  and  $i \in I_\ell$  such that

$$(3.12) \quad \tilde{f} := \sum_{\ell \in L} \sum_{i \in I_\ell} \alpha_{\ell,i} \varphi_{\ell,i} \quad \text{satisfies} \quad \tilde{f}(\mathbf{x}_{\ell',i'}) = f(\mathbf{x}_{\ell',i'}) , \quad \ell' \in L , \quad i' \in I_{\ell'} .$$

If we used the full grid  $L = \{\ell \mid \ell \leq n \cdot \mathbf{1}\}$  of some level  $n \in \mathbb{N}$ , then the problem would suffer from the curse of dimensionality: There are  $\prod_{t=1}^r (2^n - 1) \in \mathcal{O}((2^n)^r)$  grid points, a number which grows exponentially in the dimensionality  $r$ . Sparse grids aim at selecting only a subset of the levels involved in the full grid, thus drastically decreasing the grid size, while maintaining a slightly deteriorated interpolation error. For degree  $p = 1$ , it can be shown [11] that the selection of  $L := \{\ell \mid \|\ell\|_1 \leq n + r - 1\}$  leads to a grid with  $\mathcal{O}(2^n n^{r-1})$  grid points but worsens the  $L^2$  interpolation error

only slightly from  $\mathcal{O}(h_n^2)$  (full grid) to  $\mathcal{O}(h_n^2 n^{r-1})$ , where  $n^{r-1}$  is a polynomial factor in  $n$ . This leads to the common definition [11] of the regular sparse grid with level  $n$ ,

$$(3.13) \quad V_{n,r}^s := \bigoplus \{W_\ell \mid \ell \in \mathbb{N}^r, \|\ell\|_1 \leq n+r-1\}.$$

It has proven well-suited in a number of applications, even with other basis functions than the usual hat functions [10, 39, 45, 46]. The two-dimensional regular sparse grid of level 3 can be seen in Figure 2(b).

**3.4. Boundary treatment.** In our topology optimization setting, a good approximation near the boundary  $\partial[0, 1]^r$  of the parameter space  $[0, 1]^r$  is crucial: Many of the cells in the final optimization result will be either fully filled with material or empty. This means that some or all of the corresponding unit cell parameters for our chosen parametrizations shown in subsection 5.1 will be near zero or one.

The sparse grids described above do not provide a good approximation near  $\partial[0, 1]^r$ , since there will be an unnatural decay towards  $\partial[0, 1]^r$  (for  $p = 1$ , the interpolants will vanish on  $\partial[0, 1]^r$ ). The general approach is, in one dimension, to insert an additional level  $\ell = 0$  of two boundary basis functions  $\varphi_{0,i}$  and corresponding grid points  $x_{0,i}$  for  $i \in I_0 := \{0, 1\}$  (both defined via (3.3) and (3.6), respectively). This is depicted in Figure 2(a) (dashed lines). Then, the regular sparse grid with boundary points can be defined as

$$(3.14) \quad V_{n,r}^{s,1} := \bigoplus \{W_\ell \mid \ell \in \mathbb{N}_0^r, \max(\ell, \mathbf{1})\|_1 \leq n+r-1\};$$

see, e.g., [11]. The resulting sparse grids have the same resolution on the boundary as in the interior, as can be observed in Figure 2(b). This corresponds to directly inserting the boundary basis functions into level one [39] and summing all subspaces with  $\|\ell\|_1 \leq n+r-1$ , but for the sake of clarity we stick to definition (3.14).

According to [11, 20], the dimension of  $V_{n,r}^{s,1}$  is given by

$$(3.15) \quad \dim V_{n,r}^{s,1} = \sum_{m=0}^r 2^m \binom{r}{m} \dim V_{n,r-m}^s,$$

$$(3.16) \quad \dim V_{n,r}^s = \sum_{q=0}^{n-1} 2^q \binom{r+q-1}{r-1}$$

with the convention of  $\dim V_{n,0}^s = 1$  for  $n \in \mathbb{Z}$  and  $\dim V_{n,r}^s = 0$  for  $n \leq 0$  and  $r \in \mathbb{N}$ . In Tables 1 and 2, we put  $\dim V_{n,r}^{s,1}$  in relation (third column) to the number  $\dim V_{n,r}^s$ ,

TABLE 1  
Total number  $|V_{n,r}^{s,b}|$  of points in relation to the number  $|V_{n,r}^s|$  of interior points for  $r = 3$ .

$ V_{n,r}^s $	$ V_{n,r}^{s,b}  /  V_{n,r}^s $				
	$b = 1$	$b = 2$	$b = 3$	$b = 4$	$b = 5$
$n = 1$	1	27.00	9.00	9.00	9.00
$n = 2$	7	11.57	4.71	2.14	2.14
$n = 3$	31	7.26	3.39	1.84	1.26
$n = 4$	111	5.34	2.75	1.67	1.23
$n = 5$	351	4.29	2.37	1.55	1.21
$n = 6$	1023	3.63	2.13	1.47	1.19
$n = 7$	2815	3.18	1.96	1.41	1.17
$n = 8$	7423	2.86	1.83	1.36	1.16

TABLE 2

Total number  $|V_{n,r}^{s,b}|$  of points in relation to the number  $|V_{n,r}^s|$  of interior points for  $r = 10$ .

$ V_{n,r}^s $	$b = 1$	$b = 2$	$ V_{n,r}^{s,b} / V_{n,r}^s $			
			$b = 3$	$b = 4$	$b = 5$	
$n = 1$	1	59049	1025	1025.0	1025.0	1025.0
$n = 2$	21	21558	2813	49.8	49.8	49.8
$n = 3$	241	10046	1879	246.0	5.3	5.3
$n = 4$	2001	5407	1211	227.2	30.5	1.5
$n = 5$	13441	3213	806	181.1	34.7	5.4
$n = 6$	77505	2054	558	140.6	32.2	6.8
$n = 7$	397825	1390	401	109.5	28.2	7.1
$n = 8$	1862145	984	298	86.5	24.2	6.8

of inner grid points (second column) for  $r = 3$  and  $r = 10$ , respectively. Especially for higher dimensionalities, almost all points of  $V_{n,r}^{s,1}$  are on the boundary since there are  $2^m \binom{r}{m}$  many boundary faces of codimension  $m$  and on each face, there is a sparse grid of the same level  $n$  as in the interior. As in [45], we generalize the definition of  $V_{n,r}^{s,1}$  to regular sparse grids  $V_{n,r}^{s,b}$ ,  $b \in \mathbb{N}$ , which contain coarser grids on the boundary than in the interior such that for  $b = 1$  the definition is consistent with (3.14) (i.e., mesh width  $h_n$  on the boundary), for  $b = 2$  the finest mesh width on the boundary is  $h_{n-1}$ , and so on.

To motivate the definition of  $V_{n,r}^{s,b}$ , we partition the level vectors  $\boldsymbol{\ell} \in \mathbb{N}_0^r$  of (3.14) in fully interior (with  $\boldsymbol{\ell} \in \mathbb{N}^r$ ) and boundary levels (with  $\boldsymbol{\ell} \in \mathbb{N}_0^r \setminus \mathbb{N}^r$ ). Then, we limit the 1-norm of boundary level vectors to  $n + r - b$  instead of  $n + r - 1$ , treating zero levels as level one functions as before. Finally, we add  $W_0$  to our grid as we want the final grid to contain at least all  $2^r$  corners of  $[0, 1]^r$ , even if  $b$  is high (i.e.,  $b > n$ ). Otherwise, we would obtain a grid without any points on the boundary.

**DEFINITION 3.1.** We define for  $n, r, b \in \mathbb{N}$  the  $r$ -dimensional regular sparse grid  $V_{n,r}^{s,b}$  of level  $n$  with boundary parameter  $b$  as

$$\begin{aligned} V_{n,r}^{s,b} := & \bigoplus \{W_{\boldsymbol{\ell}} \mid \boldsymbol{\ell} \in \mathbb{N}^r, \|\boldsymbol{\ell}\|_1 \leq n + r - 1\} \oplus \\ & \bigoplus \{W_{\boldsymbol{\ell}} \mid \boldsymbol{\ell} \in \mathbb{N}_0^r \setminus \mathbb{N}^r, (\|\max(\boldsymbol{\ell}, \mathbf{1})\|_1 \leq n + r - b) \vee (\boldsymbol{\ell} = \mathbf{0})\}, \end{aligned}$$

where  $\max(\boldsymbol{\ell}, \mathbf{1})$  is calculated componentwise (its  $t$ th component is given by  $\max(\ell_t, 1)$ ).

Two- and three-dimensional examples for  $V_{n,r}^{s,b}$  are shown in Figure 3. Note that the definition is, when choosing  $b = 1$ , indeed consistent with (3.14) as

$$\begin{aligned} & \{\boldsymbol{\ell} \in \mathbb{N}^r \mid \|\boldsymbol{\ell}\|_1 \leq n + r - 1\} \cup \{\boldsymbol{\ell} \in \mathbb{N}_0^r \setminus \mathbb{N}^r \mid \|\max(\boldsymbol{\ell}, \mathbf{1})\|_1 \leq n + r - 1\} \cup \{\mathbf{0}\} \\ &= \{\boldsymbol{\ell} \in \mathbb{N}_0^r \mid \|\max(\boldsymbol{\ell}, \mathbf{1})\|_1 \leq n + r - 1\}. \end{aligned}$$

There is a similar relation for the number of grid points as (3.15).

**PROPOSITION 3.2.** The dimension of  $V_{n,r}^{s,b}$  is given by

$$\dim V_{n,r}^{s,b} = \dim V_{n,r}^s + \sum_{m=1}^r 2^m \binom{r}{m} \dim V_{n-b+1, r-m}^s.$$

The statement can be proven similarly to (3.15) by considering that  $V_{n,r}^{s,b}$  is the union of  $V_{n,r}^s$  as interior grid with  $V_{n-b+1, r-m}^s$  on the  $2^m \binom{r}{m}$  boundary faces of co-dimension  $m$ . A full proof can be found in Appendix A. In Tables 1 and 2, we observe

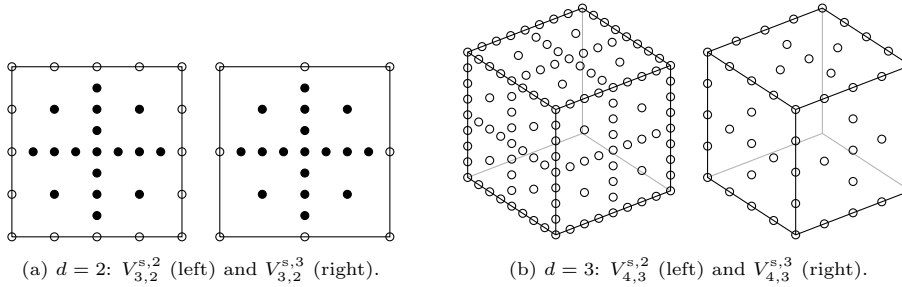


FIG. 3. Examples for  $V_{n,r}^{s,b}$  in 2D and 3D. In 3D, only the boundary points on the left, front, and top boundary face are shown.

that the ratio of total points to boundary points decreases significantly when using higher values for  $b$ , especially for  $r = 10$ . Note that in both tables, the ratio remains constant in each row as soon as  $b > n$ , since in this case  $V_{n,r}^{s,b} = V_{n,r}^s \oplus W_0$  regardless of  $b$ . A disadvantage of  $V_{n,r}^{s,b}$  is that the application of the unidirectional principle [39] for interpolating with the hat function basis is harder, though still possible. As the principle cannot be applied to B-splines anyway [44] (we interpolate by solving the corresponding linear system (3.12)), this is not too much of a concern for us.

**3.5. Spatially adaptive sparse grids.** As already mentioned, spatial adaptivity is crucial to save valuable elasticity tensor evaluations in uninteresting areas. Usually, spatially adaptive sparse grids are generated by iteratively refining single points of the grid with the aid of some refinement indicator. We start with a regular sparse grid and stop when a specific number of grid points has been reached, which is usually dictated by the computational limit and the complexity of the objection function (as we have to evaluate the objection function at every grid point). By “refining” a grid point  $x_{\ell,i}$ , we mean inserting the up to  $r + |\{t \mid \ell_t > 0\}|$  children  $x_{\ell',i'}$  with

$$(3.17) \quad x_{\ell',i'} = \begin{cases} x_{\ell,i} & \text{if } t \neq t', \\ x_{\ell_t+1,2i_t\pm 1} & \text{if } t = t' \text{ and } \ell_t > 0, \\ x_{1,1} & \text{if } t = t' \text{ and } \ell_t = 0 \end{cases}$$

into the grid, where  $t' = 1, \dots, r$ . If a point to be inserted is already in the grid, it is not inserted a second time.

One of the most common refinement criteria for the piecewise linear basis (i.e.,  $p = 1$ ) is the surplus-based criterion. In the surplus-based criterion, those grid points are refined whose hierarchical surpluses (interpolation coefficients) have high absolute values. This criterion has been studied thoroughly for the piecewise linear basis, where it has a nice motivation due to a connection of the surpluses to second mixed derivatives [11, 20, 39].

In Algorithm 3.1, we display the algorithm we use to generate the spatially adaptive sparse grids. The elasticity tensor to be interpolated is matrix-valued; we assume that all tensor entries and the porosity of the microstructure are combined into one vector-valued function  $\mathbf{f}: [0, 1]^r \rightarrow \mathbb{R}^m$ . As a result, the hierarchical surpluses  $\alpha_{\ell,i}^1$  are vector-valued, too. The superscript “1” indicates that the surpluses are calculated for the piecewise linear basis due to the theoretic motivation of the surplus-based criterion and due to efficiency reasons. We merge the entries of  $\alpha_{\ell,i}^1$  into one scalar

**Algorithm 3.1** Spatially adaptive sparse grid generation

---

```

Start with an initial grid  $V \leftarrow V_{n,r}^{s,b}$ ;
Evaluate  $f$  at all grid points  $x_{\ell,i}$ ;
while there are refinable points left do
    Hierarchize: Calculate  $\alpha_{\ell,i}^1 \in \mathbb{R}^m$  by solving system (3.12);
     $\beta_{\ell,i} \leftarrow c^\top |\alpha_{\ell,i}^1|$  for all  $(\ell, i)$  in  $V$ ;
    Adaptation: Refine  $\leq N_{\text{refine}}$  of the refinable points with the largest  $\beta_{\ell,i}$ ;
    Evaluate  $f$  at new grid points  $x_{\ell,i}$ ;
end while
return  $V$ ;

```

---

$\beta_{\ell,i}$  by taking a linear combination of their absolute values.  $\beta_{\ell,i}$  is then used as a refinement indicator. We identify basis functions and grid points with each other and denote spanned spaces  $V_{n,r}^{s,b}$  as ‘‘grids,’’ even though they do not contain the grid points. The algorithm treats an existing grid point  $x_{\ell,i}$  as ‘‘refinable’’ if  $\|\ell\|_\infty < \ell_{\max}$ ,  $\beta_{\ell,i} > \varepsilon$ , and at least one child of the form (3.17) is missing. User-given parameters are  $n, b \in \mathbb{N}$  (level and boundary parameter of the initial grid),  $c \in (\mathbb{R}^+)^m$  (surplus weights),  $N_{\text{refine}} \in \mathbb{N}$  (maximal number of points to refine per iteration),  $\ell_{\max} \in \mathbb{N}$  (maximal one-dimensional level), and  $\varepsilon > 0$  (weighted surplus tolerance).

Note that in order to efficiently evaluate the surpluses of the piecewise linear basis with the unidirectional principle, it is necessary that all indirect hierarchical ancestors (defined by inverting (3.17)) of every grid point are also contained in the grid [39, 45]. Therefore, missing ancestors are implicitly inserted in the refinement step of Algorithm 3.1.

Once we have generated the spatially adaptive sparse grid with Algorithm 3.1, we obtain the final B-spline interpolant by calculating the hierarchical surpluses  $\alpha_{\ell,i}$  on said grid for B-spline basis functions of degree  $p = 3$ .

**4. Interpolation of elasticity tensors.** We recall that the problems at the microscopic and the macroscopic level are coupled by the homogenized elasticity tensor  $E^H : [0, 1]^r \rightarrow \mathbb{R}^{6 \times 6}$  (Voigt notation applies). It relates the stress tensor  $\sigma \in \mathbb{R}^6$  to the strain tensor  $\epsilon \in \mathbb{R}^6$  by Hooke’s law:

$$(4.1) \quad \sigma = E^H \epsilon .$$

When solving the two-scale problem, a coupled approach that solves a subproblem for all requested  $E^H$  will generally result in a high computational cost, due to many repetitive local material optimizations. For that reason, we replace the computations of  $E^H$  during the optimization by evaluations of a high-dimensional surrogate function  $\tilde{E} : [0, 1]^r \rightarrow \mathbb{R}^{6 \times 6}$ , which is computed before the actual optimization takes place, i.e., in an *offline phase*. To construct  $\tilde{E}$ , we generate a spatially adaptive sparse grid, where we compute  $E^H$  at the grid points and determine the hierarchical surpluses in the piecewise linear basis for the refinement criterion. After refinement is finished, we compute the hierarchical surpluses in the cubic B-spline basis, which are the interpolation coefficients for the surrogate function. Using the surrogate does not only drastically reduce computational cost. It also has to be set up only once and can be reused in different macroscopic problem settings.

The elasticity tensor has to be positive definite as it otherwise would mimic unphysical behavior and the linear system of the finite element analysis cannot be solved.

Hence, the surrogate  $\tilde{E}$  obtained as the interpolating function has to be positive definite for all admissible  $\mathbf{x}_n$  as well. This also applies to relating tensors in other linear constitutive laws like, e.g., Darcy's law of fluid in porous media, Fourier's law of heat conduction or Fick's law of diffusion.

**4.1. Preserving positive definiteness.** Preserving the positive definiteness in the interpolation of the elasticity tensors  $E^H : [0, 1]^r \rightarrow \mathbb{R}^{6 \times 6}$  is crucial. However, conventional interpolation methods such as sparse grid interpolation do not preserve positive definiteness. Our numerical experiments show that simply interpolating  $E^H$  by a sparse grid function  $\tilde{E}$  only works for most regular sparse grids or few, specially tailored spatially adaptive ones [46]. In most other cases, oscillations of the interpolant  $\tilde{E}$  result in areas where the interpolated elasticity tensor is not positive definite anymore. As a result, the optimization process often fails without giving a reasonable optimized structure. In Figure 4(a), we depict the minimal eigenvalue for an exemplary parametrization with two parameters, which we will explain later on (see subsection 5.1). Oscillations leading to negative eigenvalues can be seen clearly.

Positivity of the diagonal of  $E^H$  is necessary for the symmetric tensor being positive definite, but the sparse grid interpolation does not preserve this positivity. This means that already oscillations of a single entry  $E_{ii}^H$  can destroy the positive definiteness of the whole interpolant  $\tilde{E}$ . When using sparse grids, such oscillations likely occur near the boundary of the parameter space, where the elasticity tensor interpolant is evaluated often (as many microstructures will either be almost empty or fully filled with material). This is a general problem for sparse grids and a direct consequence of mitigating the curse of dimensionality. Trying to manually fix the interpolation of the entries in an isolated manner, for example, by clamping them via  $\tilde{E}_{ii} \leftarrow \max(\tilde{E}_{ii}, 0)$ , does not lead to success. It is the tensor  $\tilde{E}$  as a whole whose interpolation has to be fixed.

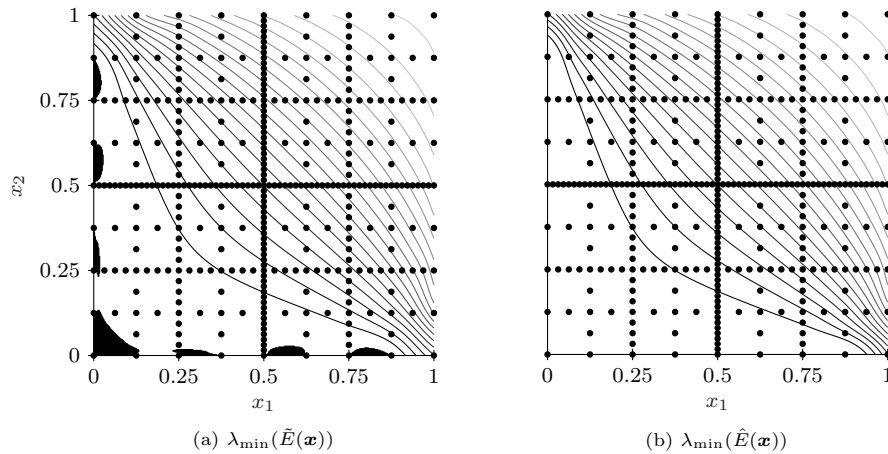


FIG. 4. Minimal eigenvalue of the elasticity tensor of the cross parametrization from Figure 6(a) that was computed by interpolating directly ( $\tilde{E}(\mathbf{x})$ , (a)) or by taking the square of the interpolated Cholesky factors ( $\hat{E}(\mathbf{x})$ , (b)). The dots are the points of the regular sparse grid of level 5, which was used for the interpolation. Areas where the minimal eigenvalue is negative are shown in black. The isoline values are separated by 0.02.

The special case of preserving positivity when interpolating a scalar function is important. One obvious application is sparse grid density estimation [18, 25], where the interpolant should be a valid density function and thus be nonnegative. Possible approaches to ensure positivity are adding some grid points to the grid [18], which only works for piecewise linear functions, or using transformations like taking the logarithm before interpolating and exponentiating the interpolant when evaluating. Potentially, these solutions may be transferred to preserve positive definiteness by taking the eigenspace transformation and preserving the positivity of the interpolated eigenvalues. However, we have developed a more canonical approach here.

**4.2. Cholesky factor interpolation.** We define  $R: [0, 1]^r \rightarrow \mathbb{R}^{6 \times 6}$  as the Cholesky factor of  $E^H$ , that is,  $R(\mathbf{x})$  is the unique upper triangular matrix with positive diagonal such that  $E^H(\mathbf{x}) = R(\mathbf{x})^\top R(\mathbf{x})$ . Such a factorization always exists as  $E^H$  is symmetric and positive definite. In each iteration of the offline grid generation phase (see Algorithm 3.1), we evaluate  $E^H(\mathbf{x}_{\ell,i})$  at the new grid points, compute the corresponding Cholesky factors  $R(\mathbf{x}_{\ell,i})$ , and hierarchize using surpluses with respect to  $R$ . In the notation of Algorithm 3.1, this means using the entries of  $R$  instead of  $E$  for the function  $f$  to be interpolated. As the result of the offline phase, we store the hierarchical surpluses of the interpolant  $\tilde{R}$  of  $R$ . In the online phase, every time the evaluation  $E^H(\mathbf{x})$  of the elasticity tensor  $E^H$  is requested, we evaluate  $\tilde{R}(\mathbf{x})$  and return  $\hat{E}(\mathbf{x}) := \tilde{R}(\mathbf{x})^\top \tilde{R}(\mathbf{x})$ .

The resulting  $\hat{E}$  is positive semidefinite and almost everywhere positive definite: The only possibility for  $\hat{E}$  being singular is when  $\tilde{R}(\mathbf{x})$  is singular, which will only be the case on a negligible null subset of  $[0, 1]^r$ . The minimal eigenvalue of  $\hat{E}$  is shown in Figure 4(b). There are no black areas anymore which would indicate negative eigenvalues.

This approach has also the advantage that like the direct interpolant  $\tilde{E}$  of  $E^H$ ,  $\hat{E}$  can still be differentiated easily via the product rule,

$$(4.2) \quad \frac{\partial}{\partial x_t} \hat{E}(\mathbf{x}) = \tilde{R}(\mathbf{x})^\top \cdot \frac{\partial}{\partial x_t} \tilde{R}(\mathbf{x}) + \frac{\partial}{\partial x_t} \tilde{R}(\mathbf{x})^\top \cdot \tilde{R}(\mathbf{x}), \quad t = 1, \dots, r,$$

since both  $\tilde{R}(\mathbf{x})$  and  $\frac{\partial}{\partial x_t} \tilde{R}(\mathbf{x})$  are known. The ability to differentiate  $\hat{E}$  is essential as this allows us to continue using gradient-based optimization. Otherwise, we would have to resort to much slower converging gradient-free optimization methods, or we would have to approximate the Jacobians by finite differences, introducing a new parameter (the distance of the finite difference evaluations) and a new error source.

**5. Numerical results and discussion.** In this section, we apply the presented method to two-scale optimization scenarios. In addition, we study interpolation errors and the effect of the interpolation of Cholesky factors on these errors. The results of this section are based on [45]. All results were computed using cubic B-splines ( $p = 3$ ).

**5.1. Settings and unit cell parametrizations.** For the presentation of results, we choose the two optimization settings shown in Figure 5. We apply a finite element scheme and discretize the two-dimensional design domain  $\Omega = [0, 2] \times [0, 1]$  uniformly into  $\mathcal{N}_{\text{cell}} = 64 \times 32 = 2048$  cells. In the three-dimensional setting, the domain is a unit cube  $\Omega = [0, 1]^3$  split uniformly into  $\mathcal{N}_{\text{cell}} = 20 \times 20 \times 20 = 8000$  cells. At the left edge (2D) or face (3D) we incorporate homogeneous Dirichlet boundary conditions, i.e., clamping. A point load acts on the domain's bottom in both settings

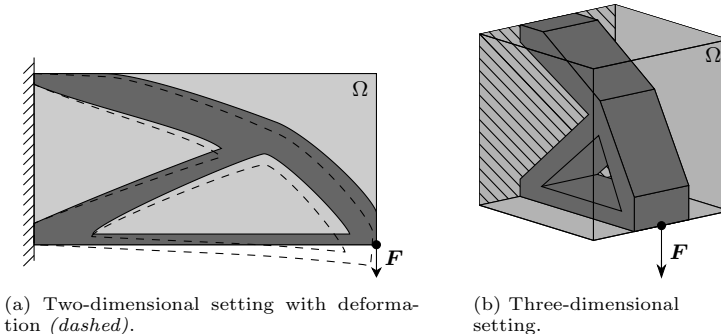


FIG. 5. Optimization settings in two and three spatial dimensions with the design domain  $\Omega$  (light gray), loads  $\mathbf{F}$ , and a possible structure layout (dark gray). Hatched areas indicate clamping boundary conditions.

(on  $(3, 0)$  in 2D and on  $(1, 0.5, 0)$  in 3D). The objective is to minimize the compliance. Thus, the discretized problem (see 2.7) reads as

$$(5.1) \quad \begin{aligned} & \min_{\mathbf{x} \in U_{ad}} \quad f^\top u \\ & \text{s.t.} \quad K(\mathbf{x})u = f, \\ & \quad V(\mathbf{x}) \leq V_0 \end{aligned}$$

with stiffness matrix  $K$ . The upper bound  $V_0$  on the material volume fraction is chosen to be 50 % of the volume of domain  $\Omega$  in 2D and 10 % in 3D. We solve problem (5.1) with SNOPT [22], which uses a sequential quadratic programming (SQP) method, and employ a density filtering method for regularization.

We use the unit cell topology parametrizations depicted in Figure 6 for two and three spatial dimensions. As basis cell in 2D we choose a cross consisting of two axes aligned orthogonal bars, where the unit cell parameters determine the widths of the bars (Figure 6(a)). Note that this also represents a microstructure with rectangular holes like in the work of Bendsøe and Kikuchi [8]. For the framed cross parametrization we add two diagonal bars (Figure 6(c)). Both of the parametrizations are extended by an additional shearing parameter (Figure 6(b) and (d)). In 3D, the basic cross parametrization with three bars (Figure 6(e)) is modified by adding two additional shearing parameters in horizontal directions (Figure 6(f)). The resulting parametrization is determined by five unit cell parameters. Note that the aforementioned parametrizations might not capture the optimal unit cell topology for most load cases. Thus, in future work we plan to employ more sophisticated parametrizations such that the dimensionality of the corresponding sparse grids will be even higher. However, for this article we restrict ourselves to these exemplary parametrizations for demonstration purpose. The cell problems are solved using a finite element method with 128 elements in each spatial dimension in (16 384 elements) and 16 elements in each spatial dimension in 3D (4096 elements), implemented in the finite element toolbox CFS++ [34].<sup>1</sup> We use the sparse grid toolbox SG++ [39] to interpolate the Cholesky factors with hierarchical B-splines on sparse grids.<sup>2</sup>

<sup>1</sup><https://cfs-doc.mdm.tuwien.ac.at/>.

<sup>2</sup><http://sgpp.sparsegrids.org/>.

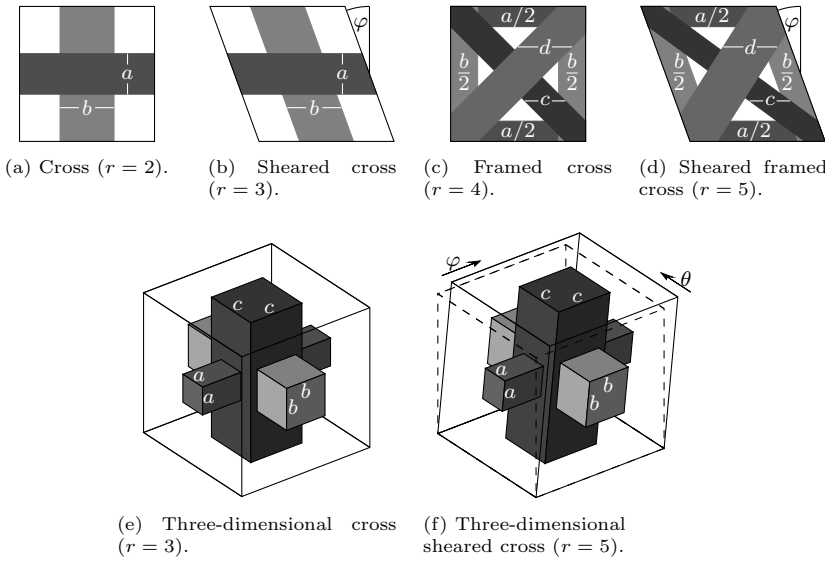
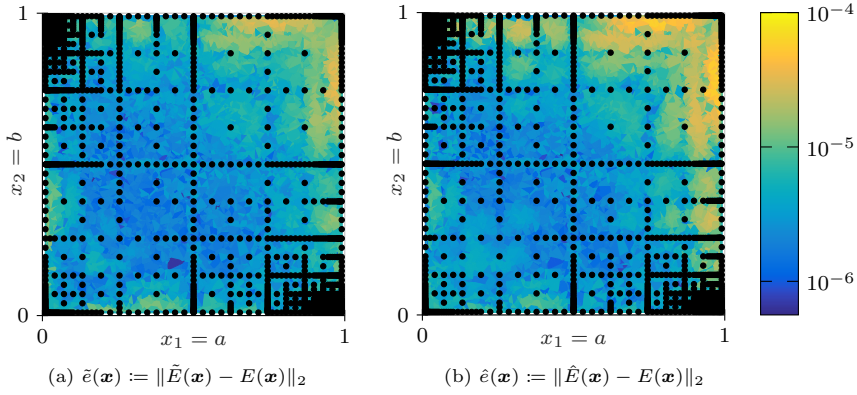


FIG. 6. Unit cell parametrizations in two and three spatial dimensions.

FIG. 7. Pointwise error of interpolating the elasticity tensor for the cross parametrization from Figure 6(a) (parameters  $\mathbf{x} = (a, b)$ ). The two figures, which share the same color scale, compare the direct interpolant  $\tilde{E}$  of the elasticity tensor  $E$  with the elasticity tensor  $\hat{E} := \tilde{R}^\top \tilde{R}$  recovered from the interpolant  $\tilde{R}$  of the Cholesky factor  $R$  of  $E$ .

**5.2. Interpolation error.** We first compare the interpolation error of directly interpolating the elasticity tensor with the interpolation error of interpolating the Cholesky factor instead. For plotting purposes, we pick the two-dimensional cross parametrization from Figure 6(c) as an example, as it has only two parameters.

In Figure 7(a), we use the elasticity tensor  $E^H$  to generate a spatially adaptive sparse grid (see subsection 3.5) consisting of 1320 points. The resulting interpolant  $\tilde{E}$  is compared to the true elasticity tensor  $E^H$  on 5000 uniform pseudorandom Monte Carlo points. As the difference  $\tilde{E}(\mathbf{x}) - E^H(\mathbf{x})$  is again a matrix, we plot the spectral norm  $\tilde{e}(\mathbf{x}) := \|\tilde{E}(\mathbf{x}) - E^H(\mathbf{x})\|_2$  on a logarithmic scale in Figure 7(a).

For the interpolation of the Cholesky factor  $R$  of  $E^H$ , we normally would generate the spatially adaptive grid based on the hierarchical surpluses of  $R$  as described in subsection 4.2. However, for comparison purposes, we use the same grid as in Figure 7(a) (which was generated using the hierarchical surpluses of  $E^H$ ). The resulting interpolant  $\tilde{R}$  is used to approximately recover the elasticity tensor by  $E^H(\mathbf{x}) \approx \hat{E}(\mathbf{x}) := \tilde{R}(\mathbf{x})^\top \tilde{R}(\mathbf{x})$ . Plotting the spectral norm  $\hat{e}(\mathbf{x}) := \|\hat{E}(\mathbf{x}) - E^H(\mathbf{x})\|_2$  of the difference to  $E^H$ , we obtain Figure 7(b). As expected by error analysis, the error increases when doing Cholesky factorization. In terms of the relative root-mean-square of the errors, we have for this example

$$\|\tilde{e}\|_{L^2}/\|e\|_{L^2} \approx 1.49 \cdot 10^{-4}, \quad \|\hat{e}\|_{L^2}/\|e\|_{L^2} \approx 4.26 \cdot 10^{-4},$$

where  $e(\mathbf{x}) := \|E^H(\mathbf{x})\|_2$ . However, this is a very moderate increase as the errors have the same order of magnitude.

We can recalculate these errors, which only belong to a single grid, for coarser and finer grids. The resulting convergence plot is given in Figure 8, which also contains the errors for the sheared cross parametrization from Figure 6(b). We infer from the plot that the additional error incurring when reconstructing the elasticity tensor approximation  $\hat{E}$  from the Cholesky factor  $\tilde{R}$  seems to be a constant factor. The order of convergence remains roughly the same.

**5.3. Compliance value.** The actual objective function  $J(\mathbf{u}(\mathbf{x}))$  is the compliance function value corresponding to the displacement for the unit cell parameter configuration  $\mathbf{x} = (\mathbf{x}_1, \dots, \mathbf{x}_{N_{\text{cell}}}) \in ([0, 1]^r)^{\mathcal{N}_{\text{cell}}}$ . For computing the displacement, we need to know the exact elasticity tensors  $E_n^H = E^H(\mathbf{x}_n)$  for each of the cells  $n = 1, \dots, N_{\text{cell}}$ , but our offline-online approach uses the interpolated elasticity tensors  $\hat{E}_n = \hat{E}(\mathbf{x}_n)$  instead (or  $\tilde{E}_n$ , if we interpolate  $E$  directly without using the Cholesky factorization). An interpolation error will of course influence the error between the actual deformation  $\mathbf{u}(\mathbf{x})$  and the one  $\tilde{\mathbf{u}}(\mathbf{x})$  computed with respect to  $\tilde{E}$  as well as the actual compliance function value and  $J(\tilde{\mathbf{u}}(\mathbf{x}))$ , which is reported by the SQP routine.

This assumption is supported by Figure 9, which visualizes the influence of the interpolation error on the reported optimized objective value  $J(\tilde{\mathbf{u}}(\mathbf{x}^*))$  and the

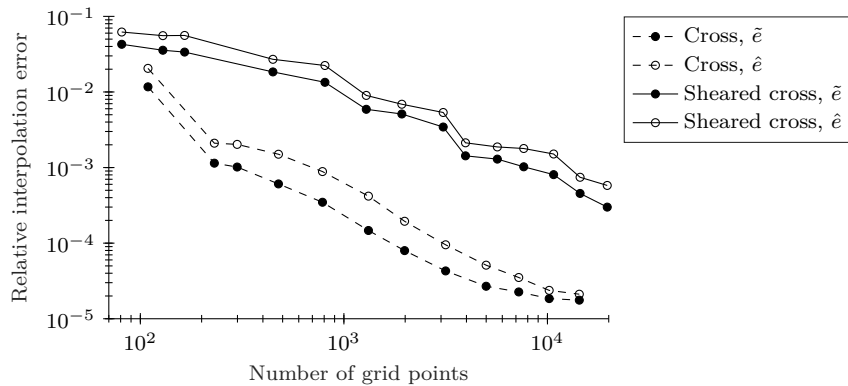


FIG. 8. Convergence of interpolation errors for the cross (see Figure 6(a)) and the sheared cross (see Figure 6(b)) parametrizations. Shown are the errors  $\tilde{e}$  for the direct interpolant  $\tilde{E}$  of  $E$  and of the errors  $\hat{e}$  for the reconstructed tensor  $\hat{E} := \tilde{R}^\top \tilde{R}$ . Normalization is done by the respective norm of  $E$ .

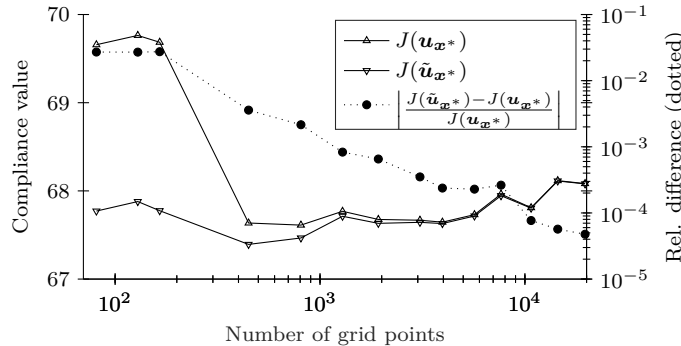


FIG. 9. Actual compliance value  $J(\mathbf{u}(\mathbf{x}^*))$ , reported compliance value  $J(\tilde{\mathbf{u}}(\mathbf{x}^*))$ , and their relative difference for the calculated optimized unit cell parameter configurations  $\mathbf{x}^*$ .

corresponding actual objective value  $J(\mathbf{u}(\mathbf{x}^*))$  for the sheared cross parametrization from Figure 6(b). Latter is obtained by computing  $E^H$  for all optimized parameter values  $\mathbf{x}^*$ , i.e., evaluating (2.5) at  $\mathbf{x}_n^*$  instead of interpolating, and calculating the objective. For the very coarse initial grid consisting of only 81 points in Figure 9, there is a large gap between reported and actual compliance. As the grid is refined and the number of grid points increases, the gap between  $J(\tilde{\mathbf{u}}(\mathbf{x}^*))$  and  $J(\mathbf{u}(\mathbf{x}^*))$  becomes smaller as the interpolation error decreases.

**5.4. Computational complexity.** In the following, we analyze the complexity of our method, which consists of three steps:

1. Offline step A (grid generation): Generation of the spatially adaptive sparse grid, evaluation of the elasticity tensor at the grid points, Cholesky factorization, repeated computation of hierarchical surpluses in the piecewise linear basis.
2. Offline step B (hierarchization): Single computation of hierarchical surpluses (interpolation coefficients) in the cubic B-spline basis.
3. Online step (optimization): Repeated evaluation of the objective function and its gradient, evaluation of sparse grid interpolant.

The expensive evaluations of the elasticity tensors in offline step A, the Cholesky factorizations, and the evaluations of the sparse grid interpolant in the online step can each be parallelized due to the embarrassingly parallel nature of the problems.

Hereinafter we consider the expenses in conducting the finite element analysis for the microporblems (2.3) and macroproblem (2.7) to be a constant factor and focus on the complexity with respect to the number of grid points  $N$  in the resulting spatially adaptive sparse grid. Thus, we can analyze the complexity of the three steps as follows: First, the asymptotic complexity of offline step A is at most  $\mathcal{O}(rN^2)$ . This is because the hierarchical surpluses in the piecewise linear basis can be computed in  $\mathcal{O}(rN)$  time with the unidirectional principle (see, e.g., [45]) and there are at most  $N$  iterations in Algorithm 3.1. Usually, Algorithm 3.1 will be much faster as up to  $N_{\text{refine}}$  points are inserted in each iteration. Second, the hierarchization step is asymptotically the most expensive step as it needs  $\mathcal{O}(N^2(N+r))$  since a general linear system (3.12) of size  $N \times N$  has to be solved [45]. Third, the online step requires

$$(5.2) \quad \mathcal{O}(N_{\text{it}}(N_J + rN_{\nabla J})\mathcal{N}_{\text{cell}}(m+1)rN)$$

time (if a single one-dimensional hierarchical basis evaluation takes constant time). Here,  $N_{\text{it}}$  is the number of optimization iterations needed to satisfy the convergence criterion of the optimizer,  $N_J$  and  $N_{\nabla J}$  are the maximum numbers of evaluations of  $J$  or  $\nabla J$  per optimization iteration,  $\mathcal{N}_{\text{cell}}$  is the number of finite elements,  $m$  is the number of distinct entries of the elasticity tensor (in general,  $m = 6$  in 2D and  $m = 21$  in 3D), and we add 1 for the porosity which is interpolated as well. Finally,  $rN$  is the number of one-dimensional basis evaluations per  $r$ -variate basis function. Hence, the computational time for the online step is linear in the number  $N$  of grid points. As the number of iterations varies for the different grids, the computational time of the online phase can be nonmonotonous. The memory complexity for the three steps is linear for offline step A and the online step, and up to quadratic for the hierarchization step (only linear if an iterative linear system solver is employed).

Computations were performed on a shared-memory computer with 4x Intel Xeon E7-8880v3 (72 cores, 144 threads) and times measured. For example, for the finest grid of Figure 9 with 19 669 points, offline step A took 22 minutes, the offline step B took 2 minutes, and the online step took 107 minutes (with 1747 iterations and 1911 evaluations of  $J$  and  $\nabla J$ ). This might seem slow at first, but using the exact elasticity tensor  $E$  instead of the surrogate  $\hat{E}$  would have implied a time-to-solution of over 11,000 minutes, if we assume that every evaluation of  $E$  takes five seconds (perfectly parallelized on 144 threads), that the number of optimization iterations stays the same, and that we account for the additional evaluations that would have to be performed to approximate the missing gradient of  $E$  by finite differences. This indicates that we achieved a speedup of around 86 by separating calculations on the micro- and macroscopic scales and using the surrogate  $\hat{E}$  instead of solving problems on the microscale. Note that this already includes the offline costs that do not have to be repeated once the elasticity tensors have been precomputed. Consequently, it is effectively infeasible to compare our surrogate-based results to the direct evaluation of the exact elasticity tensors.

This argument also applies to standard surrogates obtained by full grid interpolation. Due to the lack of spatial adaptivity, full grid interpolation would require a single level (mesh size) for each dimension. For example, a level of 7 would result in  $2^7 + 1 = 129$  equidistant grid points per dimension, i.e.,  $129^3 > 2 \cdot 10^6$  grid points in  $r = 3$  dimensions. This would increase the runtime of the online step of the finest grid of Figure 9 by two orders of magnitude. However, the corresponding sparse grid contains grid points of up to level 10, which would render the solution with full grids infeasible. Additionally, higher-dimensional parametrizations would also prohibit full grid interpolation due to the curse of dimensionality.

**5.5. Optimized structures.** In Figures 10 and 11, we see resulting optimized structures for two and three spatial dimensions, respectively. As mentioned in the introduction, some of the parametrizations lead to disconnected microstructures. A posttreatment of the optimization result would be necessary to achieve connectivity, which of course will also change the behavior, i.e., objective function value, of the structures, and a careful comparison between the original result of the optimization procedure and the posttreated structure had to be done. We ignore this circumstance in our reconstruction, where we plot each unit cell individually. The optimized two-dimensional structures look quite different for the various parametrizations of the unit cell topology. This is due to the fact that the ability to withstand forces in specific directions differs from parametrization to parametrization.

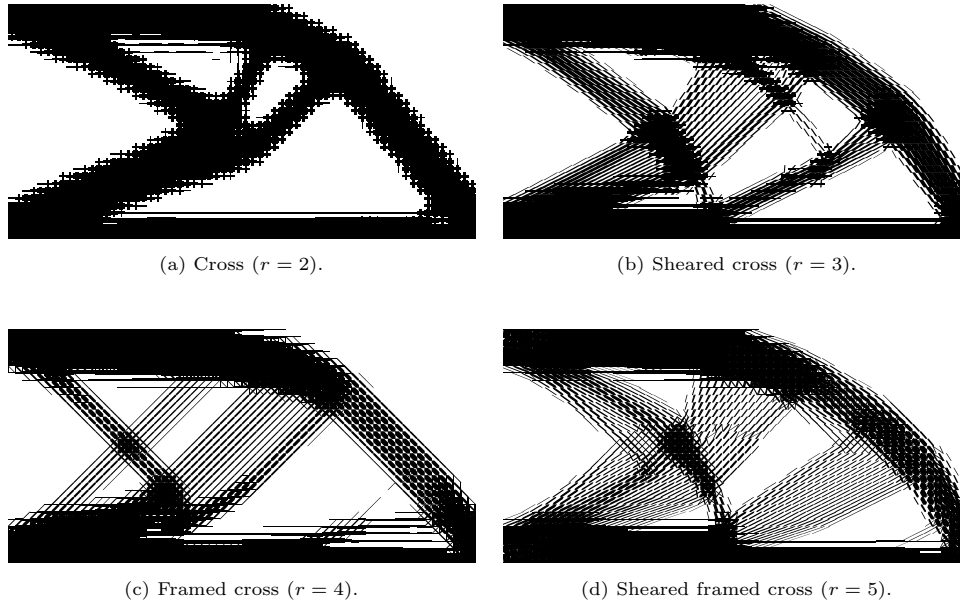


FIG. 10. Optimization results in two spatial dimensions for different unit cell topology parametrizations.

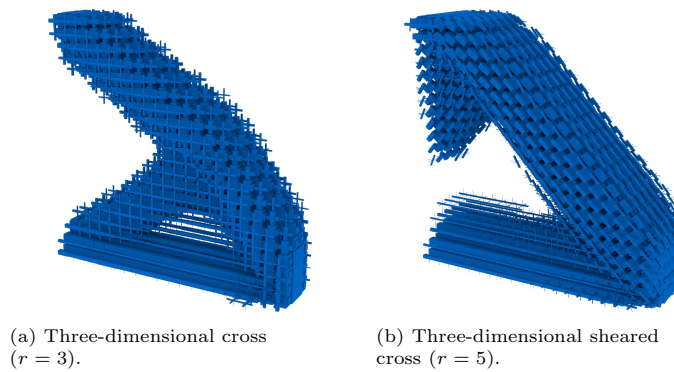


FIG. 11. Optimization results in three spatial dimensions for different unit cell topology parametrizations.

This is also reflected by the different optimized objective values  $J(\mathbf{u}(\mathbf{x}^*))$  in Table 3, which contains detailed statistics about the corresponding sparse grids and optimization processes. One can see that increasing the complexity of the parametrization (the number  $r$  of parameters) does not necessarily lead to a design with better performance, but instead the parametrization should be chosen carefully and appropriately. Also, the more complicated a parametrization is, the more grid points would of course be needed to approximate the Cholesky factors of the elasticity tensors sufficiently well. Conversely, the discrepancy between the actual and reported

TABLE 3

*Statistics for calculating the results in Figures 10 and 11. The columns denote the used parametrization, the number  $r$  of unit cell parameters, the number  $N_{\text{points}}$  of sparse grid points, the number  $N_{\text{it}}$  of outer iterations of the SQP method, the time needed for the online phase of optimization (in hours and minutes), the time needed per outer iteration (in seconds), the actual objective function value  $J(\mathbf{u}(\mathbf{x}^*))$  of the optimized parameter configuration, and the reported objective function value  $J(\tilde{\mathbf{u}}(\mathbf{x}^*))$ .*

	Parametrization	$r$	$N_{\text{points}}$	$N_{\text{it}}$	$t$ [h:mm]	$t/N_{\text{it}}$ [s]	$J(\mathbf{u}(\mathbf{x}^*))$	$J(\tilde{\mathbf{u}}(\mathbf{x}^*))$
2D	Cross	2	10 197	547	0:19	2.1	74.974	74.974
	Sheared cross	3	10 723	2196	2:13	3.6	67.809	67.804
	Framed cross	4	10 502	249	0:25	6.1	70.816	69.409
	Sheared framed cross	5	10 694	749	0:38	3.1	68.602	65.201
3D	3D cross	3	9 207	39	0:12	18.8	247.60	247.49
	3D sheared cross	5	15 389	608	4:18	25.5	162.59	159.33

objective values increases by making the parametrization more complex but keeping the number of grid points approximately constant (see Table 3).

**6. Conclusion.** In this paper, we have studied B-splines on sparse grids for gradient-based topology optimization using a two-scale homogenization approach. We have shown that using B-splines of higher degree instead of the conventional hat functions makes the use of gradient-based methods possible, which greatly benefit from the explicit availability of exact gradients. With a suitable treatment of the boundary, we have seen that surplus-based refinement techniques generate spatially adaptive sparse grids which approximate the elasticity tensors well. By calculating Cholesky factors and interpolating them instead of the actual tensors, we have preserved positive definiteness of the tensors while still being able to differentiate the surrogate explicitly. We have demonstrated that the error introduced by the Cholesky factorization is relatively small and that the convergence rates are similar. Finally, our method shows feasible and physically reasonable results in the exemplary settings, while being computed in a fairly short time.

In this article, we limited ourselves to a setting in linear elasticity and minimized the compliance subject to only one constraint (i.e., volume). In future work, this may be extended to not only more constraints but also other mechanics, for instance, problems with fluid-structure interaction, heat exchange problems, or piezoelectric materials. Additionally, it might be desired to find optimal designs for multifunctional requirements, e.g., compliant structures that have a high buckling load or are able to suppress dynamic excitations. It will then also be necessary to use more complex unit cell topology parametrizations with more parameters, and the interpolation of the homogenized material properties will become more sophisticated. Furthermore, the two-scale optimization could be conducted with different parametrizations of the unit cell in different regions of the macroscopic domain. The complexity of the parametrization might be reduced again by tailoring the unit cell parametrization to the specific requirements in those subdomains, since the parametrization of the unit cell topology does not have to account for all requirements at once. In addition, it should be possible to reduce the complexity of the hierarchization step by using different hierarchical spline bases [45]. Finally, future work could focus on a comparison of the performance of hierarchical B-splines to other sparse grid bases and to approaches that are not based on sparse grids.

### Appendix A. Proof of Proposition 3.2.

*Proof.* The dimension of  $V_{n,r}^{s,b}$  splits up into the dimension  $\dim V_{n,r}^s$  of the interior grid and the dimension of the boundary space:

$$\dim V_{n,r}^{s,b} = \dim V_{n,r}^s + \sum_{\{\boldsymbol{\ell} \in \mathbb{N}_0^r \setminus \mathbb{N}^r \mid \|\max(\boldsymbol{\ell}, \mathbf{1})\|_1 \leq n+r-b \wedge \boldsymbol{\ell} = \mathbf{0}\}} \dim W_{\boldsymbol{\ell}}.$$

The dimension of  $W_{\boldsymbol{\ell}}$  is given by  $2^{\|\boldsymbol{\ell}\|_1 - r + 2N_{\boldsymbol{\ell}}}$ , where  $N_{\boldsymbol{\ell}} := |\{t \mid \ell_t = 0\}|$  is the number of zero levels of  $\boldsymbol{\ell}$ . Note that  $\|\max(\boldsymbol{\ell}, \mathbf{1})\|_1 = \|\boldsymbol{\ell}\|_1 + N_{\boldsymbol{\ell}}$ . We split up the sum into parts of equal  $N_{\boldsymbol{\ell}}$  and equal  $\|\boldsymbol{\ell}\|_1$ :

$$\dim V_{n,r}^{s,b} = \dim V_{n,r}^s + 2^r + \sum_{m=1}^{r-1} \sum_{q=0}^{n+r-b-m} \sum_{\{\boldsymbol{\ell} \in \mathbb{N}_0^r \mid N_{\boldsymbol{\ell}} = m, \|\boldsymbol{\ell}\|_1 = q\}} 2^{q-r+2m}.$$

We count the levels  $\boldsymbol{\ell} \in \mathbb{N}_0^r$  with  $N_{\boldsymbol{\ell}} = m$  and  $\|\boldsymbol{\ell}\|_1 = q$  by first placing  $m$  zeros in  $r$  places ( $\binom{r}{m}$  possibilities) and then counting all  $(r-m)$ -vectors whose entries are positive and sum up to  $q$ :

$$\begin{aligned} |\{\boldsymbol{\ell} \in \mathbb{N}_0^r \mid N_{\boldsymbol{\ell}} = m, \|\boldsymbol{\ell}\|_1 = q\}| &= \binom{r}{m} |\{\boldsymbol{\ell} \in \mathbb{N}^{r-m} \mid \|\boldsymbol{\ell}\|_1 = q\}| \\ &= \binom{r}{m} \binom{q-1}{r-m-1} \end{aligned}$$

for  $q \geq r-m$ . For  $q < r-m$ , the inner sum vanishes, and we continue with

$$\dim V_{n,r}^{s,b} = \dim V_{n,r}^s + 2^r + \sum_{m=1}^{r-1} \binom{r}{m} \sum_{q=r-m}^{n+r-b-m} 2^{q-r+2m} \binom{q-1}{r-m-1}.$$

With an index shift  $q \rightarrow q + r - m$  and a slight rearrangement, we can apply (3.16) (together with corresponding conventions) and obtain

$$\begin{aligned} &= \dim V_{n,r}^s + 2^r + \sum_{m=1}^{r-1} 2^m \binom{r}{m} \sum_{q=0}^{n-b} 2^q \binom{(r-m)-1+q}{(r-m)-1} \\ &= \dim V_{n,r}^s + \sum_{m=1}^r 2^m \binom{r}{m} \dim V_{n-b+1, r-m}^s, \end{aligned}$$

as desired. □

**Acknowledgments.** We would like to thank the anonymous reviewers for their helpful comments.

### REFERENCES

- [1] G. ALLAIRE, *Homogenization and two-scale convergence*, SIAM J. Math. Anal., 23 (1992), pp. 1482–1518.
- [2] G. ALLAIRE, *Shape Optimization by the Homogenization Method*, Springer-Verlag, New York, 2001.
- [3] G. ALLAIRE, P. GEOFFROY-DONDERS, AND O. PANTZ, *Topology optimization of modulated and oriented periodic microstructures by the homogenization method*, Comput. Math. Appl., 78 (2019), pp. 2197–2229.

- [4] C. S. ANDREASEN AND O. SIGMUND, *Topology optimization of fluid–structure–interaction problems in poroelasticity*, Comput. Methods Appl. Mech. Engrg., 258 (2013), pp. 55–62.
- [5] C. BARBAROSIE AND A.-M. TOADER, *Shape and topology optimization for periodic problems*, Struct. Multidiscip. Optim., 40 (2009), 381.
- [6] C. BARBAROSIE AND A.-M. TOADER, *Optimization of bodies with locally periodic microstructure*, Mech. Adv. Mater. Struct., 19 (2012), pp. 290–301.
- [7] R. BELLMAN, *Adaptive Control Processes: A Guided Tour*, Princeton University Press, Princeton, NJ, 1961.
- [8] M. P. BENDSØE AND N. KIKUCHI, *Generating optimal topologies in structural design using a homogenization method*, Comput. Methods Appl. Math., 71 (1988), pp. 197–224.
- [9] M. P. BENDSØE AND O. SIGMUND, *Topology Optimization: Theory, Method and Applications*, 2nd ed., Springer-Verlag, New York, 2003.
- [10] H.-J. BUNGARTZ, *Finite Elements of Higher Order on Sparse Grids*, Habilitationsschrift, Technische Universität München, 1998.
- [11] H.-J. BUNGARTZ AND M. GRIEBEL, *Sparse grids*, Acta Numer., 13 (2004), pp. 147–269.
- [12] A. CHERKAEV, *Variational Methods for Structural Optimization*, Springer-Verlag, New York, 2000.
- [13] P. COELHO, P. FERNANDES, J. GUEDES, AND H. RODRIGUES, *A hierarchical model for concurrent material and topology optimisation of three-dimensional structures*, Struct. Multidiscip. Optim., 35 (2008), pp. 107–115.
- [14] M. G. COX, *The numerical evaluation of B-splines*, IMA J. Appl. Math., 10 (1972), pp. 134–149.
- [15] C. DE BOOR, *On calculating with B-splines*, J. Approx. Theory, 6 (1972), pp. 50–62.
- [16] J. DENG, J. YAN, AND G. CHENG, *Multi-objective concurrent topology optimization of thermo-elastic structures composed of homogeneous porous material*, Struct. Multidiscip. Optim., 47 (2013), pp. 583–597.
- [17] Z. DU, X.-Y. ZHOU, R. PICELLI, AND H. A. KIM, *Connecting microstructures for multiscale topology optimization with connectivity index constraints*, J. Mech. Design, 140 (2018), 111417.
- [18] F. FRANZELIN AND D. PFLÜGER, *From data to uncertainty: An efficient integrated data-driven sparse grid approach to propagate uncertainty*, in *Sparse Grids and Applications – Stuttgart 2014*, J. Garcke and D. Pflüger, eds., Lect. Notes Comput. Sci. Eng. 109, Springer, New York, 2016, pp. 29–49.
- [19] D. FUJII, B. C. CHEN, AND N. KIKUCHI, *Composite material design of two-dimensional structures using the homogenization design method*, Internat. J. Numer. Methods Engrg., 50 (2001), pp. 2031–2051.
- [20] J. GÄRCKE, *Sparse grids in a nutshell*, in *Sparse Grids and Applications*, J. Garcke and M. Griebel, eds., Lect. Notes Comput. Sci. Eng. 88, Springer, New York, 2013, pp. 57–80.
- [21] P. GEOFFROY-DONDERS, G. ALLAIRE, AND O. PANTZ, *3-d topology optimization of modulated and oriented periodic microstructures by the homogenization method*, J. Comput. Phys., 401 (2020), 108994.
- [22] P. GILL, W. MURRAY, AND M. SAUNDERS, *SNOPT: An SQP algorithm for large-scale constrained optimization*, SIAM Rev., 47 (2005), pp. 99–131.
- [23] R. GLOWINSKI, *Numerical simulation for some applied problems originating from continuum mechanics*, in *Trends and Applications of Pure Mathematics to Mechanics*, Springer, New York, 1984, pp. 96–145.
- [24] J. GOODMAN, R. V. KOHN, AND L. REYNA, *Numerical study of a relaxed variational problem from optimal design*, Comput. Methods Appl. Mech. Engrg., 57 (1986), pp. 107–127.
- [25] M. GRIEBEL AND M. HEGLAND, *A finite element method for density estimation with Gaussian process priors*, SIAM J. Numer. Anal., 47 (2010), pp. 4759–4792.
- [26] J. P. GROEN AND O. SIGMUND, *Homogenization-based topology optimization for high-resolution manufacturable microstructures*, Internat. J. Numer. Methods Engrg., 113 (2018), pp. 1148–1163.
- [27] J. GUEDES, E. LUBRANO, H. RODRIGUES, AND S. TURTELTAUB, *Hierarchical optimization of material and structure for thermal transient problems*, in *IUTAM Symposium on Topological Design Optimization of Structures, Machines and Materials*, Springer, New York, 2006, pp. 527–536.
- [28] C. HABERMANN AND F. KINDERMANN, *Multidimensional spline interpolation: Theory and applications*, Comput. Econ., 30 (2007), pp. 153–169.
- [29] K. HÖLLIG AND J. HÖRNER, *Approximation and Modeling with B-Splines*, SIAM, Philadelphia, 2013.

- [30] S. J. HOLLISTER AND N. KIKUCHI, *A comparison of homogenization and standard mechanics analyses for periodic porous composites*, Comput. Mech., 10 (1992), pp. 73–95.
- [31] X. HUANG, S. ZHOU, Y. XIE, AND Q. LI, *Topology optimization of microstructures of cellular materials and composites for macrostructures*, Comput. Materials Sci., 67 (2013), pp. 397–407.
- [32] D. HÜBNER, *Mehrdimensionale Parametrisierung der Mikrozellen in der Zwei-Skalen-Optimierung*, Master's thesis, Department of Mathematics, FAU Erlangen-Nürnberg, 2014.
- [33] V. JIKOV, S. KOZLOV, AND O. OLENIK, *Homogenization of Differential Operators and Integral Functionals*, Springer-Verlag, New York, 1994.
- [34] M. KALTENBACHER, *Advanced simulation tool for the design of sensors and actuators*, in Procedia Engineering 5, Proc. Eurosensors XXIV, Linz, Austria, September 2010, pp. 597–600.
- [35] N. LAVROV, K. LURIE, AND A. CHERKAEV, *Non-uniform rod of extremal torsional stiffness*, Mech. Solids, 15 (1980), pp. 74–80.
- [36] L. LIU, J. YAN, AND G. CHENG, *Optimum structure with homogeneous optimum truss-like material*, Comput. Struct., 86 (2008), pp. 1417–1425.
- [37] B. NIU, J. YAN, AND G. CHENG, *Optimum structure with homogeneous optimum cellular material for maximum fundamental frequency*, Struct. Multidiscip. Optim., 39 (2009), p. 115.
- [38] O. PANTZ AND K. TRABELSI, *A post-treatment of the homogenization method for shape optimization*, SIAM J. Control Optim., 47 (2008), pp. 1380–1398.
- [39] D. PFLÜGER, *Spatially Adaptive Sparse Grids for High-Dimensional Problems*, PhD thesis, Technische Universität München, 2010.
- [40] H. RODRIGUES, J. M. GUEDES, AND M. P. BENDSØE, *Hierarchical optimization of material and structure*, Struct. Multidiscip. Optim., 24 (2002), pp. 1–10.
- [41] O. SIGMUND, *Design of Material Structures Using Topology Optimization*, PhD thesis, Department of Solid Mechanics, Technical University of Denmark, 1994.
- [42] R. SIVAPURAM, P. D. DUNNING, AND H. A. KIM, *Simultaneous material and structural optimization by multiscale topology optimization*, Struct. Multidiscip. Optim., 54 (2016), pp. 1267–1281.
- [43] K. SUZUKI AND N. KIKUCHI, *A homogenization method for shape and topology optimization*, Comput. Methods Appl. Mech. Engng., 93 (1991), pp. 291–318.
- [44] J. VALENTIN, *Hierarchische Optimierung mit Gradientenverfahren auf Dünngitterfunktionen*, master's thesis, IPVS, University of Stuttgart, Germany, 2014.
- [45] J. VALENTIN, *B-Splines for Sparse Grids: Algorithms and Application to Higher-Dimensional Optimization*, PhD thesis, IPVS, University of Stuttgart, Germany, 2019.
- [46] J. VALENTIN AND D. PFLÜGER, *Hierarchical gradient-based optimization with B-splines on sparse grids*, in Sparse Grids and Applications – Stuttgart 2014, J. Garcke and D. Pfüger, eds., Lect. Notes Comput. Sci. Eng. 109, Springer, New York, 2016, pp. 315–336.
- [47] W. VOIGT, *Lehrbuch der Kristallphysik (mit Ausschluss der Kristalloptik)*, Leipzig, Berlin, Teubner, 1910.
- [48] L. XIA AND P. BREITKOPF, *Multiscale structural topology optimization with an approximate constitutive model for local material microstructure*, Comput. Methods Appl. Mech. Engng., 286 (2015), pp. 147–167.
- [49] J. YAN, G.-D. CHENG, AND L. LIU, *A uniform optimum material based model for concurrent optimization of thermoelastic structures and materials*, Internat. J. Simul. Multidiscip. Design Optim., 2 (2008), pp. 259–266.
- [50] X. YAN, X. HUANG, Y. ZHA, AND Y. XIE, *Concurrent topology optimization of structures and their composite microstructures*, Comput. Struct., 133 (2014), pp. 103–110.